UNIVERSITY OF CALIFORNIA SAN DIEGO

Synthesis-Structure-Property Relations in Additively Manufactured Materials

A Thesis submitted in partial satisfaction of the requirements
for the degree Master of Science

in

Mechanical Engineering

by

Edmund Kwok Lun Lau

Committee in charge:

Professor Maziar Ghazinejad, Chair
Professor Javier Garay, Co-Chair
Professor Abhishek Saha

2022

The Thesis of Edmund Kwok Lun Lau is approved, and it is acceptable in quality and form for publication on microfilm and electronically.

University of California San Diego

2022

TABLE OF CONTENTS

LIST OF FIGURES

LIST OF TABLES

LIST OF ABBREVIATIONS

AM	Additive manufacturing
CNF	Carbon nanofibers
DMA	Dynamic mechanical analysis
EBSD	Electron back scatter detection
MEMS	Micro-electro-mechanical systems
MWCNT	Multi-walled carbon nanotubes
P1	Annealing profile 1, 1050 C for one hour
P2	Annealing profile 2, 1100 C for one hour fifteen minutes
PAN	Polyacrylonitrile
PBF	Powder-bed fusion
S-N	stress – number of cycles to failure
S-S	Stress – strain
SS	Stainless steel
SEM	Scanning electron microscopy
SLM	Selective laser melting
TEM	Transmission electron microscopy

ACKNOWLEDGEMENTS

I would like to acknowledge Professor Maziar Ghazinejad for his support and guidance as my Principal Investigator. He has helped push for many resources that were used for this research, and he has taught me a great deal through his expertise in material science and mechanics.

I would like to thank Tom Chalfant and the MAE machine shop staff allowing access to their facilities and supporting my research. They have provided great advice and had given me the creative freedom needed to complete my project.

I would like to also thank our collaborators Dr. Eugene Olevsky and Donald Olumor for supporting this project by providing their valuable resources in additive manufacturing for us.

Chapter 1 uses material found in “Distinct Roles of Tensile and Compressive Stresses in Graphitizing and Properties of Carbon Nanofibers”, 2021. Yujia Liu, Edmund Lau, Dario Mager, Marc J. Madou, Maziar Ghazinejad, Micromachines 2021, 12, 1096. The thesis author was a contributing author of this paper.

ABSTRACT OF THE THESIS

Synthesis-Structure-Property Relations in Additively Manufactured Materials

by

Edmund Kwok Lun Lau

Master of Science in Mechanical Engineering

University of California San Diego, 2022

Professor Maziar Ghazinejad, Chair
Professor Javier Garay, Co-Chair

The relationship between synthesis, structure, and mechanical properties of additively fabricated materials are studied in this thesis. The goal is to determine how mechanical treatments during or post synthesis of the material can affect its microstructure and overall performance when compared to traditionally manufactured materials. Chapter 1 details how mechanical manipulation during fabrication can affect the graphitic and mechanical properties of electrospun carbon fibers. The fibers are characterized through tensile tests, Raman

spectroscopy, and transmission electron microscopy. The carbon nanofibers have been found to have improved strength and stiffness when subjected to compressive stresses during the fabrication process when compared to untreated and tensile-treated samples.

In chapter 2, we describe how shot-peening additively manufactured 316L stainless steel samples affects its mechanical properties. The post-processed samples are characterized through tensile and fatigue tests to study the effect of surface compression on their mechanical behavior. Static and dynamic mechanical behaviors have been found to significantly benefit from the surface cold working, increasing tensile strength by 20% and fatigue life up to tenfold.

Scanning electron microscopy allowed us to analyze the microstructure of the different samples in both 316L and the carbon nanofibers. The data collected is used to corroborate how the mechanical treatments of the samples have affected material behavior and structure. Developing insight into how these materials react to their respective mechanical treatments can help influence the methods in which they are produced, giving way to stronger and more efficient materials for load-bearing and structural applications.

INTRODUCTION

Additive processes have become one of the fastest-growing manufacturing methods in today's technology. Interest in utilizing additive processes is ever increasing in many areas, such as in the medical, aerospace, and semiconductor industries [1-5]. It is important to understand the fundamental differences between additive fabrication and manufacturing (AM) and traditional manufacturing to validate its continuing emergence and how it can eventually replace traditional methods (such as casting or hot-drawing). The understanding of synthesis-structure-property relations of AM materials can build more confidence in these materials for more critical applications, such as structural and load bearing applications.

The subtle details in manufacturing and post processing of the materials can cause major variation in microstructure, and consequently their mechanical properties [4-8]. For example, when aluminum is cast, its microstructure tends to have more impurities and homogenous grain distribution. Conversely, when aluminum is forged it would have tighter, more oblong-shaped grains that intertwine with one another [9, 10]. These different microstructures yield vastly different mechanical properties, as cast aluminum would have a lower tensile strength value but higher ductility, and forged aluminum would be stronger and harder, but more brittle. Altogether, the key differences in their material properties and structures stem from their synthesis processes, which is why it is important to understand additive manufacturing's microstructural impacts on resulting material characteristics .

In addition to investigating the effect of additive manufacturing on microstructure, gaining insights into how mechanical treatments on the synthesis or post-synthesis of a material affect its microstructure and properties is beneficial for having industry-ready, AM fabricated parts [4]. Since additive manufacturing is based on the principle of layering tiny particles and

building bottom-up, it is difficult to control the grain structure that may emerge from the process [5, 11]. By studying how mechanical treatments can influence a material's microstructure before, during, or after synthesis, the microstructure can be manipulated to better serve the application that the material is intended to be used for. An example of such a trend is increased ductility in annealed metals due to its homogenized grain structure compared to increased tensile and yield strength like in forged metals [9-10, 12]. In this thesis, the static and dynamic mechanical properties of AM 316L stainless steel (SS), built by selective laser melting (SLM), are studied. Polyacrylonitrile-based carbon nanofibers (PAN CNF), built by electrospinning, are also studied for their tensile characteristics. The effects of mechanical treatments on their microstructures and mechanical performance are also investigated for both materials. We will be establishing synthesis-structure-property relations in additively fabricated materials using a host of characterization techniques, such as scanning electron microscopy (SEM) and tensile testing. Microstructure and fracture characteristics are analyzed through SEM and the tensile tests will provide stress-strain (S-S) curves that will describe the mechanical properties of each sample.

CHAPTER 1

A key theme in my MEMS and microfabrication studies is introducing mechanical treatment and electrohydrodynamic forces during the manufacturing of carbon nanofibers (CNF) to tailor their microstructures and properties. The sensors and MEMS that are fabricated with these "engineered carbons" exhibit outstanding characteristics that are desired for energy storage, electrochemical sensors [13], and medical devices [14]. Furthermore, our recent study demonstrates the impact of different mechanical stresses on the composition and mechanical properties of resulting carbon fabrics, offering attractive manufacturing routes to engineer functional graphitic carbons for device integration [1, 3]. In this chapter, we will go over how the applied stresses during synthesis of the CNF can alter its resulting microstructure. Methods such as Raman spectroscopy, scanning electron microscopy (SEM), transmission electron microscopy (TEM), and tensile tests are used to characterize the effects of the applied mechanical treatment.

Polyacrylonitrile (PAN) mixed with multi-walled carbon nanotubes (MWCNT) are used as the carbon precursor in the electrospinning process. In this synthesis method, a homogeneous solution of the aforementioned polymers is dispersed continuously out of a metal, fine-tipped syringe. A 15 kV potential was applied between the syringe and an aluminum, rotating drum, creating a potential difference between them. The polymer solution is drawn out of the syringe via electrohydrodynamic forces and pulled onto the rotating drum as the liquid vaporizes in the air. An illustration of this phenomenon is shown in figure 1.1.

The as-spun mat is divided into three identical pieces, with each piece receiving a different mechanical treatment or no treatment. One sample is mechanically pressed for 30 seconds at 120° C under 5.88 MPa of pressure then subjected to stabilization in an oven for 6 hours at 280° C. The tensile treated sample was pulled using microscope slides that were clipped

to both ends and a weight hung off of it. The approximate stress on the sample is 52.43 kPa. This sample then undergoes stabilization while under stress. The final sample goes straight to the stabilization phase after being spun as-is. All mats are then pyrolyzed in a nitrogen gas environment. They are heated to 300° C at a rate of 4.5° C per minute and held for an hour to bake away any moisture or impurities. The setpoint temperature was then raised to 1000° C at 2.5° C per minute and held at the setpoint for an hour before cooling down to ambient temperature [1].

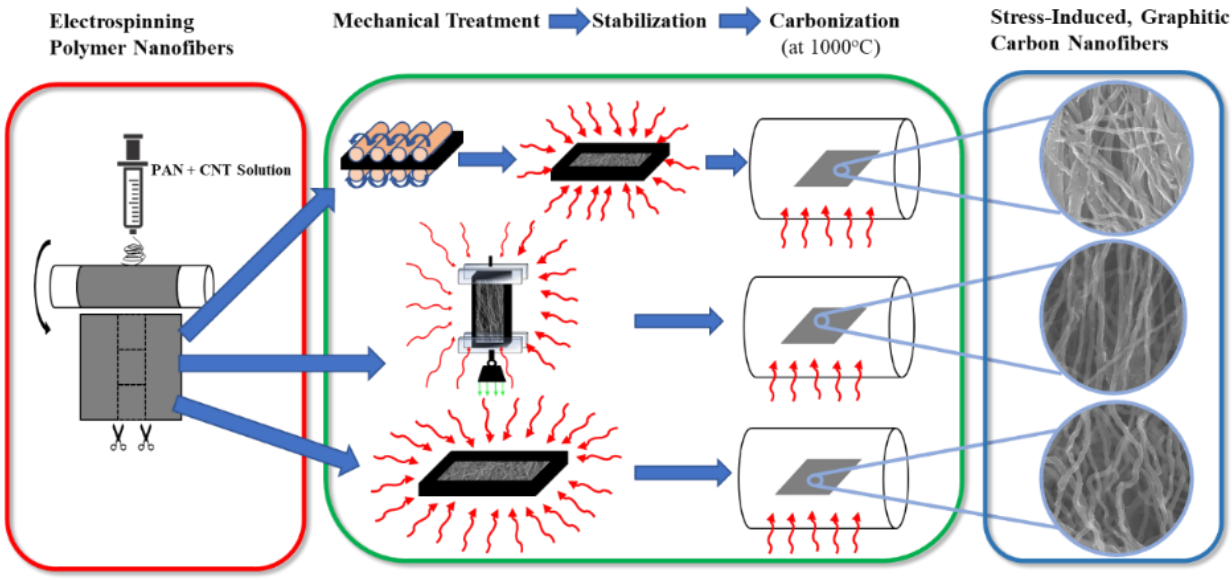

Figure 1.1: Image of the carbon nanofiber fabrication process, going from the electrospun mat, to the thermomechanical processing for each sample. The end shows the resulting morphology of the fibers due to the fabrication method [1].

Each of the carbon nanofiber samples are characterized through Raman spectroscopy, dynamic mechanical analysis, and transmission and scanning electron microscopy. Scanning electron microscopy helps us determine how the different treatments had affected the morphology of the carbon nanofibers. Figure 1.2 illustrates the differences that the mechanical treatment has had on the alignment of the nanofibers through SEM. In figure 1.2a, the untreated

fiber is more crooked and shows a vague pattern of alignment. The average fiber diameter of this sample is around 267 nm. Figure 1.2b shows that the tensile-induced sample has qualitatively improved alignment, with more fibers appearing to be much straighter and more consistent. These fibers are measured to have an average diameter of 241 nm, which is less than the untreated fiber sample. Figure 1.2c shows improved alignment and straightness of the fibers that have undergone the compression treatment. Figure 1.2c also suggests that the compression treatment of the PAN fibers has influenced more cross-linking between individual fibers. This causes the average fiber diameter to increase, with it measuring at an average of 378 nm. The thickness of each carbon fiber mat was measured to see how they were affected by the mechanical treatments. The measured thickness for the untreated, tension treated, and compression treated samples are 0.213 mm, 0.196 mm, and 0.036 mm, respectively. The thickness of the tension-induced fiber mat is less than the untreated sample, which corroborates the thinner diameter fiber from the tension-induced sample compared to the untreated sample. The compression-induced sample thickness is significantly reduced compared to untreated and tension-induced samples, indicating that the compression sample has increased density and a closer network of nanofibers, which can also be seen in figure 1.2c [1].

To further investigate the microstructure of the carbon nanofibers, we employ transmission electron microscopy (TEM). TEM allows us to gain high-resolution images of the nanofibers, providing nano-scale insights into the carbons' microstructure. Figure 1.3 shows high-resolution TEM images of compression-induced, tension-induced, and untreated carbon nanofibers. It is visibly noticeable that the compression and tension induced carbon microstructures in figure 1.3a and 1.3b show improved alignment of carbon planes over the untreated sample in figure 1.3c. The compression-induced carbon fringes also appear to show

more alignment when compared to the tension-induced sample, where the carbon fringes of the tension-induced sample seem to be more broken up and less orderly. The untreated sample's microstructure shown in figure 1.3c exhibits much greater disorder and haphazard orientations in the carbon planes.

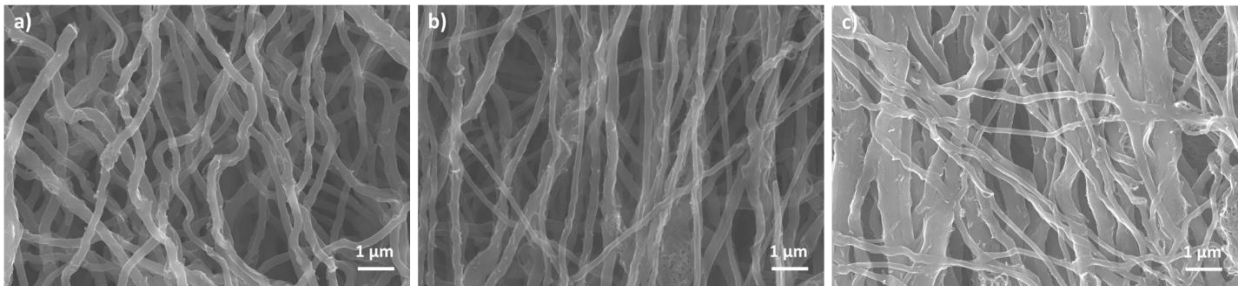

Figure 1.2: SEM images of the carbon nanofiber samples. (a) shows the untreated fiber, (b) shows the tension treated, and (c) shows the compression treated fiber [1].

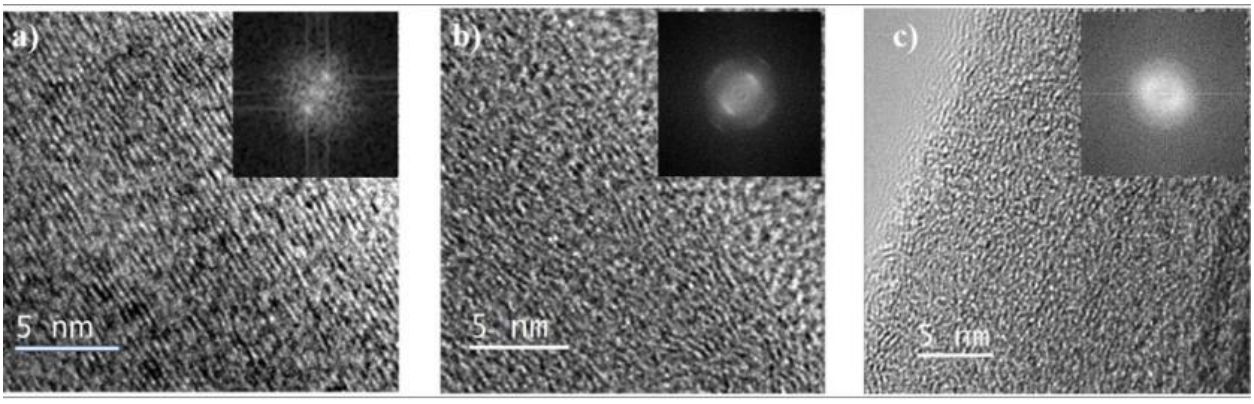

Figure 1.3: High-resolution TEM images of PAN-based carbons: (a) compression-induced pyrolytic carbon, (b) tension-induced pyrolytic carbon, and (c) untreated carbon [1].

Raman spectroscopy allows us to analyze the graphitic quality of our stress-induced carbon samples, as shown in figure 1.4. Our main interested from these graphs are the values associated with the D and G curve peaks, shown with the blue and pink dots, respectively. The shape and intensity of the G peak represents the graphitic quality and crystallinity of the sample, while the D peak represents the disorder within the sample and is associated with defects and

divergence from the graphitic carbon structure [1]. A lesser ratio between the D peak and G peak, I_D/I_G, translates to a carbon sample that is more graphitic in structure and quality. For the tension-induced sample, we see an I_D/I_G ratio of 1.13, while the compression-induced sample gives an I_D/I_G ratio of 0.71. This data shows that the compression-induced sample has superior graphitic quality compared to the tension-induced fibers, leading to higher C-C bond content and a more graphitic structure. This result is consistent with the TEM images shown in figure 1.3a and 1.3b, where the carbon fringes in the compression-induced sample presented better microstructure characteristics than the tension-induced sample. The tension-induced sample's inferior graphitic quality could be a result of the presence of microtears within the PAN fibers prior to pyrolysis. The presence of partial or full microtears, which is inevitable due to the nature of the mechanical treatment, will locally relieve tension within the nanofibers around the tear and cause the mechanical alignment of their molecular chains to be ineffective [1]. Amorphous carbon areas would then result from the subsequent stabilization due to the crosslinking of unaligned chains. The compression treatment allowed the fibers to stay intact and crosslink between each other and create a strong graphitic network.

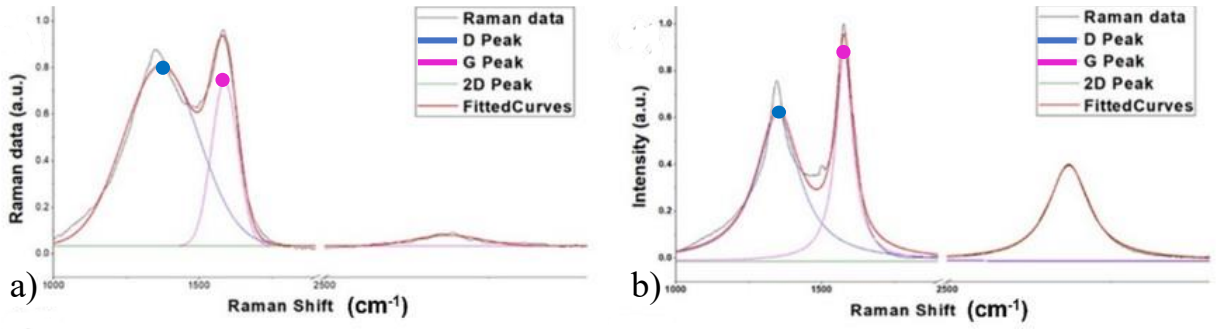

Figure 1.4: Raman Spectra of (a) tension-induced carbons and (b) compression-induced carbons [1].

Mechanical characterization is one of the most tangible synthesis-structure-property relationships we can study of a material. Using dynamic mechanical analysis (DMA), we

obtained the mechanical properties of each sample of carbon, including the tensile strength, elastic modulus, and ductility. The main focus when analyzing a material's mechanical characteristics is the stress-strain (S-S) curve produced from the DMA. Standard tensile stress-strain tests were performed on each strip, with the definition of stress used as F/A, where F is the force applied in Newtons and A is the cross-sectional area. A controlled ramp rate of 1 N/min was applied to the samples until failure.

Figure 1.5 shows three representative stress strain curves for the different carbon samples discussed. Each sample was clamped as shown on figure 1.5b and loaded in tension until failure. From the S-S curves in figure 1.5a, it is clearly shown that the elastic modulus is vastly greater in the compression-induced sample compared to the tension-induced and untreated samples, with an elastic modulus of E_c = 2.703 GPa. The tension-induced sample showed a mild increase in stiffness with an E_T = 98 MPa compared to the untreated sample, showing an elastic modulus of E_{untr} = 92 MPa. This trend is also seen in the ultimate tensile strength of the three samples. The tested compression-induced sample had a tensile strength $S_{UT,C}$ = 4.095 MPa, nearly 500% increase from the measly $S_{UT,untr}$= 0.846 MPa tensile strength of the untreated sample. The tension-induced sample also showed a 67% increase tensile strength, with $S_{UT,T}$ = 1.420 MPa. Lastly, ductility was shown to dramatically decrease in the compression-induced sample compared to the tension-induced and untreated samples. Ductility is defined as the percent strain at failure. Compression-induced carbon was shown to fail at just 0.21%, while tension-induced and untreated samples have a ductility of 1.71% and 1.03%, respectively. This phenomenon is expected as the nature of the compression treatment causes the carbon fiber to be more brittle, allowing it to have such high tensile strength and elastic modulus compared to the other samples. Another contributing factor to the improved strength and stiffness of the compression-induced

carbon could be its greater graphitic structure shown from Raman spectroscopy, mentioned earlier. Table 1.1 summarizes the mechanical properties of the three carbon samples.

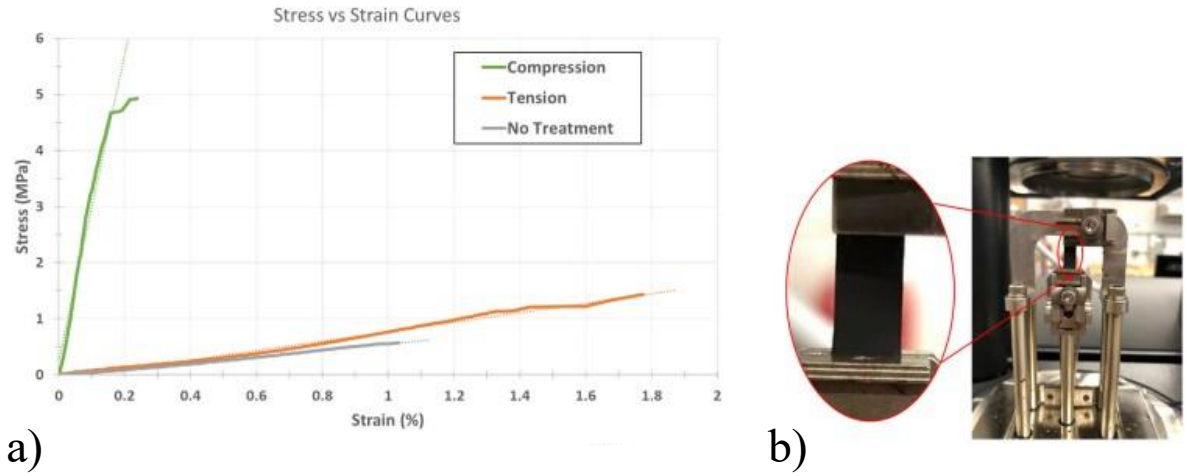

Figure 1.5: (a) Representative S-S curves of all three carbon samples (b) Photo of DMA with carbon nanofiber mat attached to tensile test fixtures [1].

Table 1.1: Mechanical properties of the three carbon samples, deduced from the S-S curve [1]

Mechanical Property	*Untreated*	*Tension-Treated*	*Compression-Treated*
Elastic Modulus, E (GPa)	0.092 ± 0.035	0.098 ± 0.069	2.703 ± 0.689
Ultimate Tensile Strength, S_U (MPa)	0.846 ± 0.252	1.420 ± 0.548	4.095 ± 1.615
Ductility, $\varepsilon_{failure}$ (% strain at failure)	1.028 ± 0.185	1.709 ± 0.684	0.210 ± 0.100

With the data from table 1.1, we can relate the results to the morphology of the different carbon samples seen under SEM. Figure 1.2b of the tension-induced sample showed that the tensile treatment had enhanced alignment of the nanofibers. This improved alignment is a likely factor in the sample's increased strength and elasticity when compared to the untreated sample. Conversely, the compression-induced fibers in figure 1.2c have shown inter-fiber cross-linking and the formation of denser fiber networks. This leads to a more rigid and less porous 2D carbon

framework, resulting in the significant increase in strength and stiffness. However, this increased rigidity also comes at the cost of decreased ductility, as a small tear in the carbon network can propagate easier, resulting in failure at lower strains compared to the tension-induced and untreated samples.

The morphological, structural, and mechanical characterizations presented in this thesis suggest that the morphology, alignment, and graphitization of carbon nanofibers are a few of the main contributors to the mechanical properties of stress-induced carbons. A relationship between synthesis, structure, and property of the carbon nanofibers is highly suggested, as differently fabricated carbon samples have exhibited vastly different results, each with their own benefits. By further investigating the mechanisms that influence carbon fiber performance, processing techniques can be developed to cater the manufactured fiber to specific needs, whether it be in the semiconductor or aerospace industry. There are numerous other mechanical characteristics not mentioned in this study, such as fracture toughness, rigidity, resilience, etc. Further study in how the mechanical treatments of the electrospun fibers affect these other mechanical properties would be needed to fully characterize the different sample types and their full benefits. This current study provides an introduction to how different mechanical treatments on the synthesis of carbon nanofibers can affect its microstructure and how that translates to its mechanical behaviors.

Acknowledgements

Chapter 1 uses material as found in Distinct Roles of Tensile and Compressive Stresses in Graphitizing and Properties of Carbon Nanofibers, 2021. Yujia Liu, Edmund Lau, Dario Mager, Marc J. Madou, Maziar Ghazinejad, Micromachines 2021, 12, 1096. The thesis author was a contributing author of this paper.

CHAPTER 2

The growing interest in metal additive manufacturing (AM) has resulted in significant growth of this industry. Several dedicated research groups investigate new methods of metal printing and how they can expand the types of metal that can be additively manufactured [4-5, 11-12, 15-17]. With the ever-expanding repertoire of methods and materials, it is imperative to study the mechanical properties of 3D printed metals to better understand the viability of these newer manufacturing methods, especially for dynamic load-bearing and structural applications. In this work, we focus on 316L stainless steel (SS), a common metal with widespread application. The microstructures and mechanical properties of AM 316L SS produced by powder bed fusion (PBF) selective laser melting (SLM), are investigated to better understand the static and dynamic mechanical behavior of AM metals. Electron backscatter detection (EBSD) allows us to analyze the grain size and microstructure of the AM 316L. To investigate AM 316L's bulk

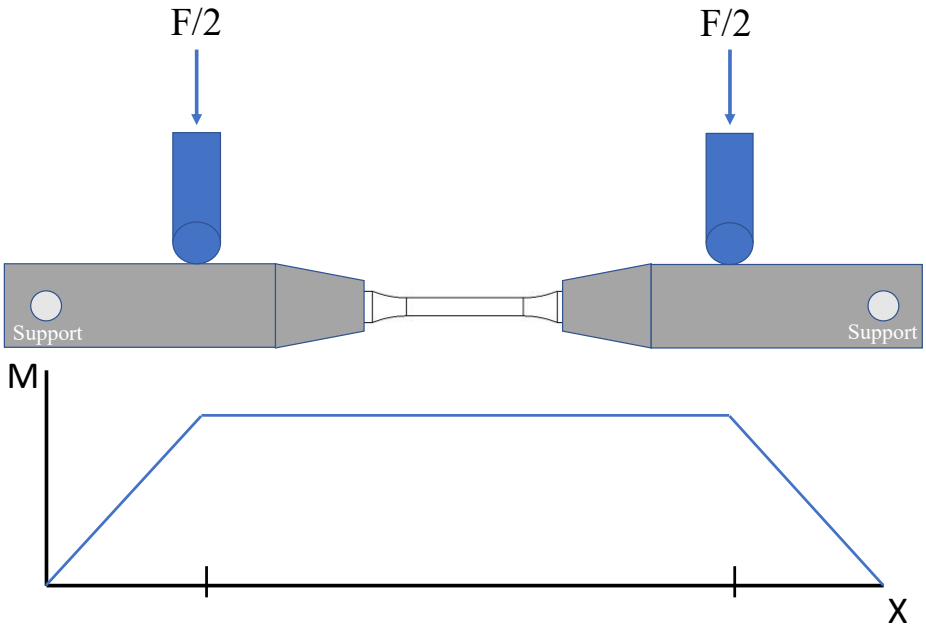

Figure 2.1: Schematic of the 4-point bending RR Moore fatigue tester with moment diagram. Moment across the fatigue specimen is constant, giving a more accurate and reliable result.

mechanical properties, we use a tensile tester with an external extensometer to acquire stress – strain (S – S) curves. Finally, we implement 4-point bending fatigue tests (RR Moore test) shown in figure 2.1 to characterize low and high life cycle fatigue.

The strength of metals is heavily dependent on their corresponding microstructure and how cracks form within them. Grain structure and size influences dislocation movement, which is how defects such as voids and inclusions are likely to become sites of crack initiation within the material. Dislocation slip predominantly occurs along grain boundaries, gradually building up and propagating until stress concentrations become too great for the material to handle and fracture occurs. It is known that smaller grained materials are both stronger and harder than larger grained materials due to the increase of grain boundary area, which impedes dislocation movement. The Hall-Petch equation describes the relationship between yield strength and grain size, where σ_y is yield stress, σ_o and k_y are material constants, and d is the average grain diameter. From the Hall-Petch equation, grain size inversely relates to yield stress and thus tensile stress [7, 8].

$$\sigma_y = \sigma_o + k_y d^{-1/2} \quad (1)$$

The impediment of slip within the microstructure slows down the propagation of cracks through the material. Cracks can be formed from chips or imperfections on the surface, inclusions such as voids or second-phase particles, or at grain boundaries, as shown in figure 2.2 [7]. For a material such as 316L stainless steel, which has little to no carbon content (<0.03 at%), there is very little second-phase particles that can cause stress concentrations and form cracks within the bulk material. Therefore, the majority of crack formation in 316L SS would be bound to occur along the surface or along grain boundaries. With crack nucleation having a high dependency on the surface, the study of surface treatments can provide advantageous insights

into the necessary processes to make 3D printed metals industry ready. This chapter focuses on the mechanical treatment of shot-peening on 316L and how it affects the microstructure and mechanical behaviors in both static and dynamic settings.

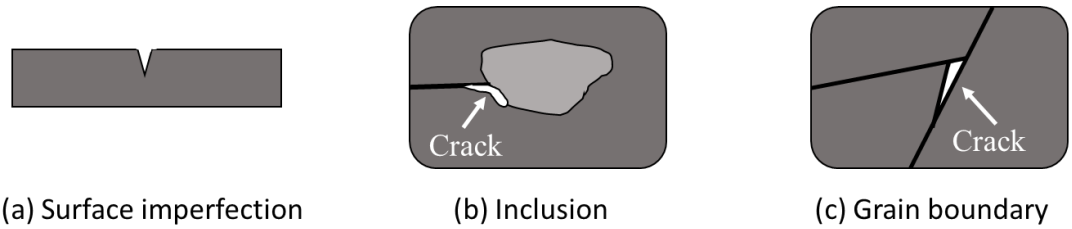

Figure 2.2: Illustration of how cracks could form **(a)** along the surface, **(b)** at inclusions, **(c)** at grain boundaries.

Various additively manufactured samples were tested in a tensile load frame to determine their stress - strain curves, including as-printed, annealed, and shot-peened . The shot-peening process bombards a material with small metal balls, forcing high levels of compression on the outer surface, as shown in figure 2.3. This results in a compressive residual stress on the surface that reduces surface grain size and holds them tightly together. The presence of residual stress and the reduction in grain size increases tensile strength, as crack nucleation on the surface becomes much more difficult to achieve [7]. Two annealing profiles are also performed on the shot-peened samples. For annealing profile 1, denoted as P1, the samples are placed in a furnace at 1050 C for one hour and left to air-cool inside. For annealing profile 2, denoted as P2, the samples are placed in a furnace at 1100 C for one hour and fifteen minutes and left to air-cool inside. The geometry of the tensile dogbone specimen follows the guidelines under ASTM E8 for a subsize specimen, shown in figure 2.4 [18].

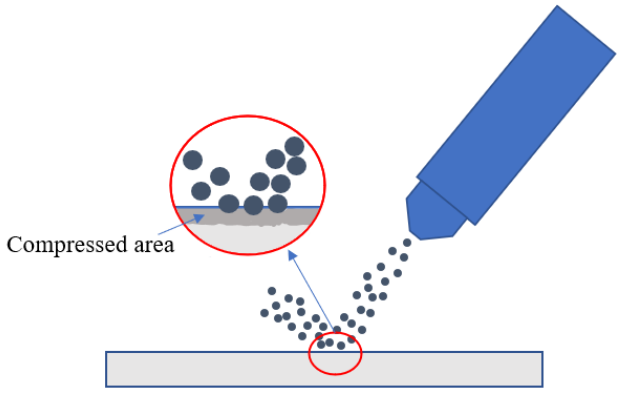

Figure 2.3: Image of shot-peening process on the surface of a metal.

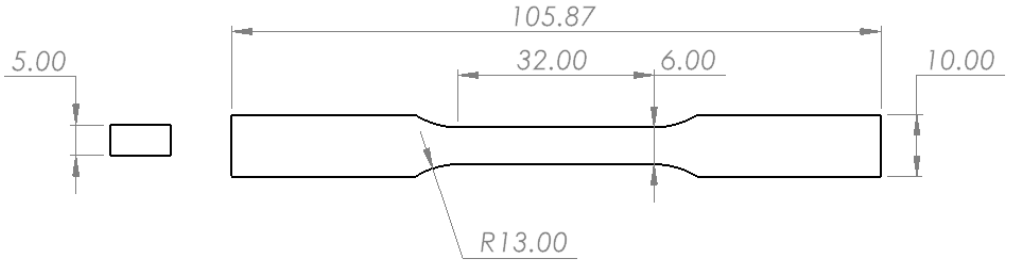

Figure 2.4: Drawing of ASTM E8 subsize specimen geometry used for tensile testing, dimensions in millimeter.

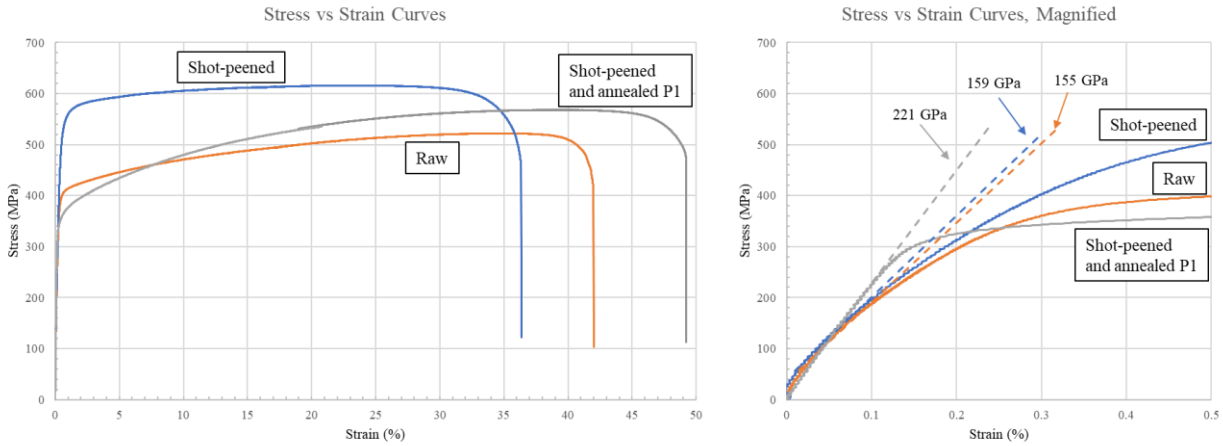

Figure 2.5: Stress – strain curves of untreated (in orange), shot-peened (in blue), and shot-peened and annealed P1 (in gray) tensile samples with expanded view from 0 – 0.5% strain for elastic modulus.

Table 2.1: Tensile test data of AM 316L SS for untreated , shot-peened, shot-peened and annealed P1, and shot-peened and annealed P2 samples.

	Ultimate Tensile (MPa)	*Elastic Modulus (GPa)*	*Yield (MPa)*	*Ductility (%)*	*Hardness (HRB)*
Material Value	515	193	205	60	80
Untreated	506 ± 10	131 ± 19	377 ± 7	35.7 ± 4.4	75.9 ± 4.2
Shot-peened	616 ± 3	155 ± 10	508 ± 15	36.5 ± 0.5	94.8 ± 1.1
Shot-peened, P1	577 ± 5	230 ± 40	370 ± 14	49.4 ± 0.4	85.3 ± 1.6
Shot-peened, P2	566 ± 7	223 ± 12	308 ± 8	54.3 ± 0.3	81.8 ± 2.9

Table 2.1 shows the significance of shot-peening on the tensile properties of AM 316L SS, with a 19% increase in ultimate tensile strength and a 32% increase in yield strength compared to untreated AM 316L SS, while having similar elastic modulus and ductility. Annealing profiles P1 and P2 still presented a 12% and 9% increase in ultimate tensile strength, respectively, and an increase in elastic modulus of over 40% for both. Ductility also improves due to annealing, with an increase of 28% and 41% respectively. Yield strength changes drastically as the annealing time and temperature increases, indicating that the samples may have needed a longer annealing time for the grains of the shot-peened AM 316L to recover and recrystallize. These differences in mechanical properties are visually demonstrated in the S – S curves in figure 2.5.

SEM micrographs of traditionally manufactured and annealed P1 316L SS, shot-peened AM 316L SS, and shot-peened and annealed P1 AM 316L SS are shown in figure 2.6. The traditionally manufactured sample is cold-drawn, which is one of the industry standards for manufacturing the 316L rods used as our baseline. Average grain sizes of these samples were found to be 17.3 μm, 9.4 μm, and 9.6 μm, respectively, which shows that the shot-peened samples have a greatly reduced average grain size, approximately by 50%. This reduction in grain size correlates to the higher tensile strength, as found in the tensile test data in table 2.1.

While the Hall-Petch equation usually refers to the relationship between grain size and yield strength, we have found that the ultimate tensile strength versus grain size of the different samples is consistent with the Hall-Petch equation as well. This means that as grain size decreases, tensile strength increases.

Figure 2.7 shows the grain structure of the same samples at their edge, clearly illustrating the effect of shot-peening on the surface. The grain structure of traditionally manufactured 316L is approximately uniform and similar in size in the inner and edge segments of the grains. Conversely, shot-peened samples of both unannealed and annealed show a layer of grains along the surface that are much smaller than the average bulk grain size. Effects of annealing are prevalent here as the layer of crushed grains in figure 2.7c are visually larger than the crushed grains in figure 2.7b. However, the annealing profile was not enough to completely reverse the shot-peening effect, resulting in still-improved tensile characteristics compared to traditional 316L SS. This effect is corroborated by observation in figure 2.8, where the fracture areas of annealed P1 AM and traditionally manufactured 316L tensile samples were analyzed under SEM. The size and formation of the micro-voids that represent a ductile fracture is significantly smaller in the AM tensile sample versus in the traditionally manufactured tensile sample.

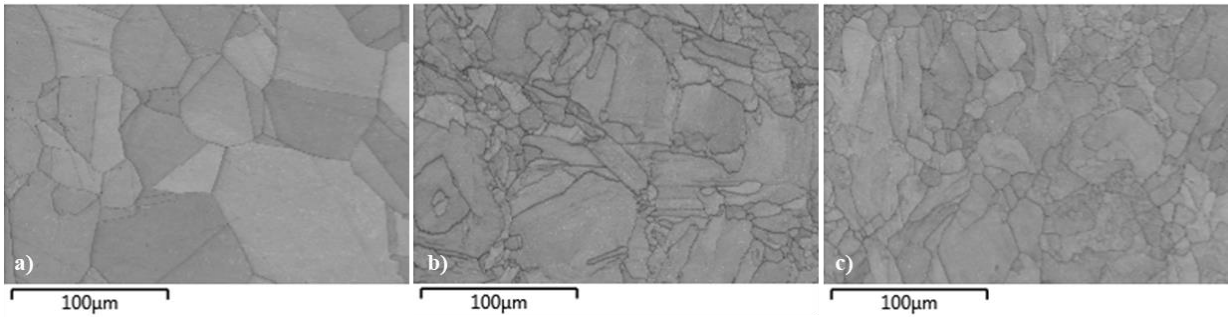

Figure 2.6: SEM micrographs of the grain structure of: **a)** traditionally manufactured and annealed P1 316L SS rod, **b)** shot-peened AM 316L SS, and **c)** shot-peened and annealed P1 AM 316L SS

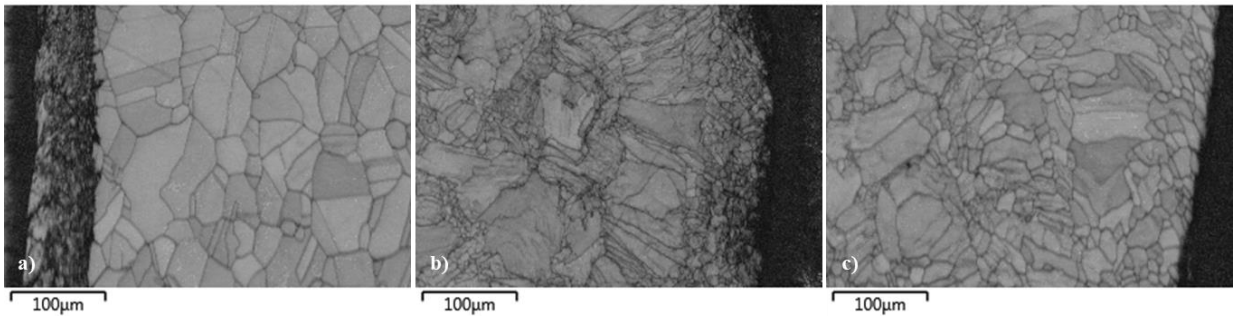

Figure 2.7: SEM micrographs of the grain structure at the edge of: **a)** traditionally manufactured and annealed P1 316L SS rod, **b)** shot-peened AM 316L SS, and **c)** shot-peened and annealed P1 ALM 316L SS

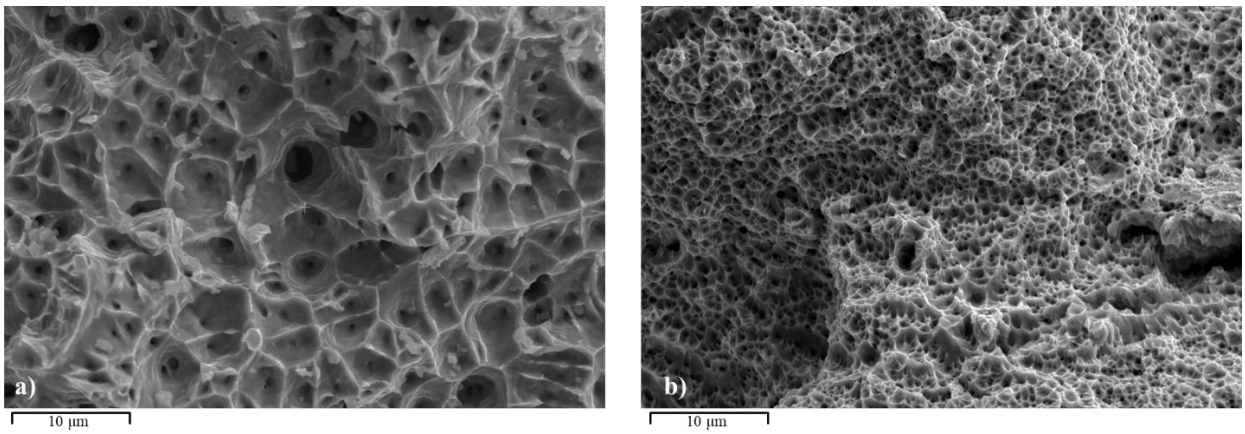

Figure 2.8: SEM images of tensile fracture areas of: **a)** traditionally manufactured and annealed P1 316L SS and **b)** annealed P1 AM 316L SS

Exploring the dynamic behavior of AM materials is critical for applying AM to structural and load bearing designs [4, 19-21]. In order to understand how AM metals deal with cyclic loading, we applied the standard 4-point rotating beam fatigue test (R. R. Moore) to determine fatigue strength characteristics of AM 316L SS. Fatigue strength is affected by the nucleation of cracks and grain boundary slip within the material perpendicular to the direction of load. The surface of materials is where cracks are most likely to start, due to the ease of slip between grain boundaries and imperfections. Defects in the microstructure such as inclusions and voids are also common areas for stress concentrations to form, initiating crack growth, as was shown in figure 2.2. For a low-carbon material such as 316L SS, there are very few inclusions within the material

that could be hot spots for crack initiation. Therefore, the fatigue strength of AM 316L SS is dependent mainly on crack initiation at the surface. Shot-peening has been shown to increase fatigue life due to its treatment on the surface of metals, since it reduces surface slip and the chance for surface crack nucleation due to the compressive residual stress left in the smaller grains along the surface [7]. Tests were performed at both 400 MPa and 500 MPa and include sample types such as cold-drawn and annealed P1 316L SS with a ground surface, untreated SLM 316L SS, shot-peened SLM 316L SS with and without a polished surface, and shot-peened and annealed P1 SLM 316L SS with a ground surface.

Life cycle expectancies of the 316L SS were calculated using the following set of equations,

$$N = \left(\frac{\sigma_{rev}}{a}\right)^{1/b}, \qquad a = \frac{(f\,S_{ut})^2}{S_e}, \qquad b = -\frac{1}{3}\log\left(\frac{f\,S_{ut}}{S_e}\right) \qquad (2, 3, 4)$$

where σ_{rev} is the completely reversed stress during testing, or the stress amplitude, f is the fatigue strength fraction, S_{ut} is the ultimate tensile strength, and S_e is the endurance limit or fatigue strength. S_e is calculated by the Marin equation,

$$S_e = k_a k_b k_c k_d k_e k_f S_e' \qquad (5)$$

where the k_i variable denotes the Marin modification factors and S_e' is half of the ultimate tensile strength [6]. In the calculation, the size factor $k_b = 1$ since the test diameter is considered small for the normal range of calculating k_b, the load and temperature factors $k_c = k_d = 1$ since the load is under complete bending and the test was performed at room temperature, and the reliability and miscellaneous effects factors $k_e = k_f = 1$ for simplicity. Therefore, the only Marin factor accounted for in this calculation is surface condition, k_a. Using equations 2-5, we can estimate the expected life cycle for our samples at specific stress amplitudes.

Table 2.2: Life cycle expectancies at 400 and 500 MPa of various samples, as calculated by equations 2, 3, and 4. Values for f found from figure 6-18 of [6]

Sample	f	S_{ut} *(MPa)*	S_e *(MPa)*	a	b	N_{400} *(cycles)*	N_{500} *(cycles)*
Traditionally manufactured, annealed P1, ground	0.89	515	239.3	877.9	-0.0941	4251	397
Untreated, unpolished	0.89	517	140.3	1508.9	-0.1719	2258	617
Untreated, ground	0.89	517	240.1	881.6	-0.0941	4427	414
Shot-peened, unpolished	0.86	616	140.4	1998.3	-0.1922	4314	1351
Shot-peened, polished	0.86	616	308	911.2	-0.0785	35826	2088
Shot-peened, annealed P1, ground	0.87	577	265.5	949.0	-0.0922	11744	1044

The estimated cycles to failure for the different samples in table 2.2 shows the significance surface condition has on fatigue life. The calculations, however, do not account for mechanical surface treatments, such as shot-peening. The only apparent effect shot-peening has on fatigue life is due to the increased ultimate tensile strength, which would increase the fatigue strength for that sample. From figures 2.7b and 2.7c, the 60 – 80 μm layer of compressed grains seen in the shot-peened samples can act to impede slip between grain boundaries near the surface, effectively minimizing the possibility of cracks nucleating on the surface. This can result in significant increases in fatigue life compared to traditionally manufactured and untreated AM 316L SS, which is illustrated in figure 2.9.

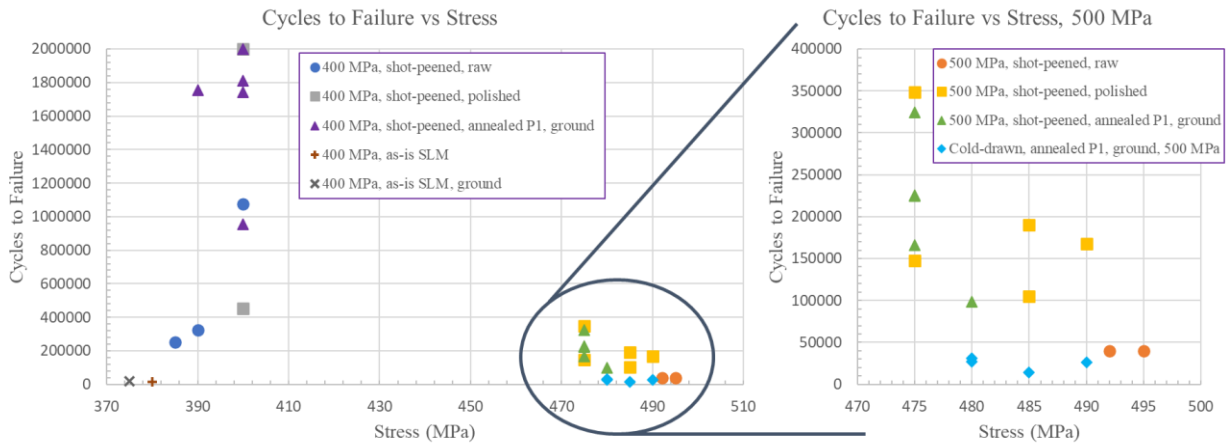

Figure 2.9: Plot of 4-point bending rotating beam fatigue tests at 400 and 500 nominal stress amplitudes to failure.

Figure 2.9 plots the cycles to failure for each test specimen. The data is organized in clusters with the target nominal stress being 400 and 500 MPa. The average alternating stress for specimens may vary slightly around the nominal stress values due to the nature of the equipment. The lower end of stresses that the specimen experienced is used as the alternating stress to give a more conservative approach in analyzing the data. The fatigue life of each sample type was estimated using equations 2-5. The Marin equation was calculated using the ultimate tensile strength found in our tensile data for each sample, so each S_e was found accordingly as listed in table 2.2. The data shows that all shot-peened samples had outlasted their estimated fatigue life significantly, with some specimens reaching what is considered infinite life (>10^6 cycles). It is also observed that the surface condition and topography on the shot-peened samples can impact their fatigue life. Unpolished samples were shown to fail with fatigue life cycles of an order of magnitude smaller (10^5 vs 10^6) than the polished or ground shot-peened samples. The shot-peened samples all outlived the untreated SLM 316L SS and the traditionally manufactured 316L SS significantly more, displaying the effect that shot-peening has on fatigue strength and dynamic behavior. Given that the maximum fatigue strength (best case scenario) for steel alloys

follows as $S_e = \frac{1}{2}S_{ut}$, we calculate our S_e = 308 MPa. Fatigue tests of ground and polished shot-peened samples had gone beyond their nominal endurance limit with an alternating stress of 400 MPa, with some going beyond one million cycles and approaching the infinite life region ($>10^6$ cycles) [6]. Even at the nominal 500 MPa alternating stress, well above the yield stress for most samples, the tests still ran far in the high cycle fatigue regime ($>10^3$ cycles) when they were estimated to run just beyond the high cycle threshold. Overall, shot-peening AM 316L SS seems to have a huge benefit in its fatigue behavior, making this mechanical post treatment extremely favorable for any structural or load bearing applications.

SEM micrographs of the fracture areas of shot-peened fatigue samples, both annealed P1 and unannealed, show that the failure-causing crack had propagated from the surface and through the bulk of the material. Due to the completely reversed loading nature of the 4-point bending rotating beam fatigue tester, it is likely that the specimen could have cracks nucleated at opposite ends of the surface and have them propagate towards the center. This phenomenon is shown in figure 2.10, where we see beech marks indicating to cracks forming on opposite sides of the specimen. It is also seen that a crack had initiated within the sample, possibly when one of the surface cracks had propagated to a non-parallel crack already within the specimen and created a stress concentration. Figure 2.10b shows the specimen experiencing ductile failure after it has reached its limit. The SEM micrographs show that even with the shot-peening treatment on the surface of the material, the specimen still had crack nucleation along the surface. This specimen was part of the shot-peened, unpolished sample, so the imperfections along the surface could still serve as crack nucleation sites. However, with the shot-peening process, the fatigue life characteristics of the specimen is still improved compared to the traditionally manufactured specimen with a ground surface. By combining polishing with the shot-peening treatment, the

fatigue life benefit is substantial compared to the polishing of a traditional specimen by reducing the likelihood of crack nucleation and propagation from the surface even more.

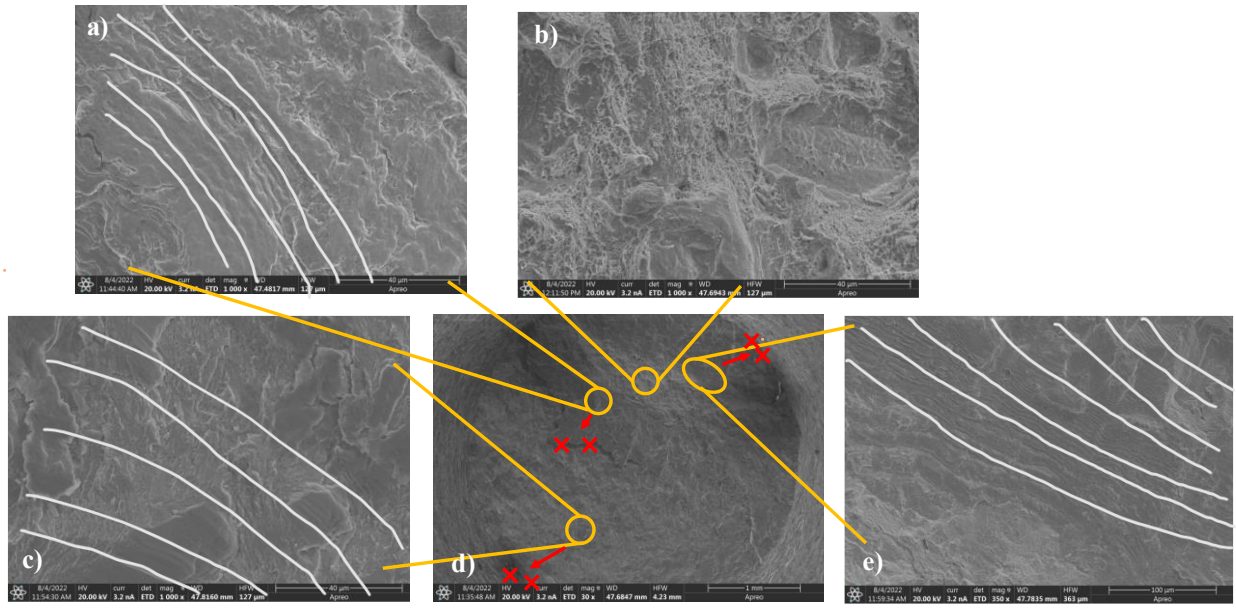

Figure 2.10: SEM micrographs of the fracture area of a shot-peened and unpolished fatigue specimen under completely reversed loading. **a, c, e)** shows propagated beech marks within the sample. **b)** shows the ductile region at failure. **d)** shows the different locations within the sample from which a-c, e were taken. Also shows areas where the crack could have initiated from.

In this chapter, the static and dynamic behavior of AM 316L SS was investigated to study how AM materials stand up compared to their traditional counterparts and how mechanical treatments, namely shot-peening, would have an effect on their microstructure and mechanical performance. It was shown that AM 316L as-printed can have similar characteristics to its traditional counterpart, but the process of shot-peening had greatly increased its tensile and fatigue properties. This could bring a lot more favorability for AM metals to be used as structural and load bearing components if the cost and convenience of additive manufacturing and shot-peening together outweigh that of traditional manufacturing. Further research in how these processes can affect other common AM metals, such as aluminum $AlSi_{10}Mg$, can expand the practical use and confidence in this new age of manufacturing to more critical applications.

Moving forward, the next steps in studying the effects of mechanical surface treatments such as shot-peening on mechanical characteristics of additively manufactured metals would be applying these treatments to metals with high internal inclusions, such as high-carbon steels. With defects within the bulk of the material, the effects of shot-peening may not have as pronounced of an effect on the fatigue behavior, as the material would have internal sources for crack nucleation. By studying the effect of shot-peening on high-carbon steels, we can better understand how different mechanical treatments can affect different additively manufactured metals and what types of post-processing will be most beneficial in supporting their mechanical properties.

REFERENCES

1. Liu, Y.; Lau, E.; Mager, D.; Madou, M.J.; Ghazinejad, M. Distinct Roles of Tensile and Compressive Stresses in Graphitizing and Properties of Carbon Nanofibers. Micromachines 2021, 12, 1096.

2. Maitra, T.; Sharma, S.; Srivastava, A.; Cho, Y.K.; Madou, M.J.; Sharma, A. Improved graphitization and electrical conductivity of suspended carbon nanofibers derived from carbon nanotube/polyacrylonitrile composites by directed electrospinning. Carbon N. Y. 2012, 50, 1753-1761.

3. Ghazinejad, M.; Holmberg, S.; Pilloni, O.; Oropeza-Ramos, L.; Madou, M. Graphitizing Non-graphitizable Carbons by Stress-induced Routes. Sci. Rep. 2017, 7, 1-10.

4. Wang, Z.; Yang, S.; Huang, Y.; Fan, C.; Peng, Z.; Gao, Z. Microstructure and Fatigue Damage of 316L Stainless Steel Manufactured by Selective Laser Melting (SLM). Materials 2021, 14, 7544.

5. Vafadar, A.; Guzzomi, F.; Rassau, A.; Hayward, K. Advances in Metal Additive Manufacturing: A Review of Common Processes, Industrial Applications, and Current Challenges. Appl. Sci. 2021, 11, 1213.

6. Budynas, R.; Nisbett, J. K.; Shigley's Mechanical Engineering Design, Tenth Edition. McGraw-Hill Education 2015.

7. Meyers, M. A.; Chawla, K. K.; Mechanical Behavior of Materials, Second Edition. Cambridge University Press 2009.

8. Callister, W. D.; Rethwisch, D. G.; Materials Science and Engineering, An Introduction, Ninth Edition. John Wily & Sons, Inc 2014.

9. Narain, V.; Ray, S. Comparative Study of Mechanical Properties of Cast and Forged Al-3Mg-MnO2 and Al-8Mg-MnO2 Composites. Heliyon 2020, 6, 1.

10. Birol, Y.; Ilgas, O. Effect of Cast and Extruded Stock on Grain Structure of EN AW 6082 alloy Forgings.Materials Science and Technology 2014, 30, 7.

11. Plessis, A.; Yadroitsava, I.; Yadroitsev, I. Effects of Defects on Mechanical Properties in Metal Additive Manufacturing: A Review Focusing on X-ray Tomography Insights. Materials and Design 2020, 187.

12. Sames, W. J.; List, F. A.; Pannala, S.; Dehoff, R. R.; Babu, S. S. The Metallurgy and Processing Science of Metal Additive Manufacturing. International Materials Reviews 2016, 61, 5.

13. Holmberg, S.; Ghazinejad, M.; Cho, E.; George, D.; Pollack, B.; Perebikovsky, A.; Ragan, R.; Madou, M.J. Stress-activated Pyrolytic Carbon Nanofibers for Electrochemical Platforms. Electrochimica Acta 2018, 290, 639.

14. Perebikovsky, A.; Hwu, A. T.; Yale, A.R.; Ghazinejad, M.; Madou, M. J. Nanofibrous Carbon Multifunctional Smart Scaffolds for Simultaneous Cell Differentiation and Dopamine Detection. ACS Biomaterials Science & Engineering 2020, 6, 225-234.

15. Fayazfar, H.; Salarian, M.; Rogalsky, A.; Sarker, D.; Russo, P.; Paserin V.; Toyserkani, E. A Critical Review of Powder-based Additive Manufacturing of Ferrous Alloys: Process Parameters, Microstructure and Mechanical Properties. Materials and Design 2018, 133, 98-128.

16. Li, C.; Liu, Z. Y.; Fang, X. Y.; Guo, Y. B. Residual Stress in Metal Additive Manufacturing. Conference on Surface Integrity 2018, 71, 348-353.

17. Singh, G.; Missiaen, J. M.; Bouvard, D.; Chaix, J. M. Additive Manufacturing of 17-4 PH Steel using Metal Injection Molding Feedstop: Analysis of 3D Extrusion Printing, Debinding and Sintering. Additive Manufacturing 2021, 47.

18. ASTM E8/E8M – 13a Standard Test Methods for Tension Testing of Metallic Materials, ASTM 2013.

19. Herliansyah, M. K.; Dewo, P.; Soesatyo, M.; Siswomihardjo, W. The Effect of Annealing Temperature on the Physical and Mechanical Properties of Stainless Steel 316L for Stent Application. 4th International Conference on Instrumentation, Communications, Information Technology, and Biomedical Engineering (ICICI-BME) 2015.

20. Gockel, J.; Sheridan, L.; Koerper, B.; Whip, B. The Influence of Additive Manufacturing Processing Parameters on Surface Roughness and Fatigue Life. International Journal of Fatigue 2019, 124, 380-388.

21. Romano, S.; Bruckner-Foit, A.; Brandao, A.; Gumpinger, J.; Ghidini, T.; Beretta, S. Fatigue Properties of AlSi10Mg obtained by Additive Manufacturing: Defect-based Modelling and Prediction of Fatigue Strength. Engineering Fracture Mechanics 2018, 187, 165-189.